Chapter 5

Core-excited states leading to the high-spin band structure in ^{93}Nb nucleus

5.1 Introduction

In previous literature, an isomeric lifetime of 1.5μs above the 37/2$^-$ level in ^{93}Nb has been predicted along with an oblate collective rotational dipole band. Thus, it was necessary to verify that the isomer exists or not above 37/2 within our scope of observation. In recent times, extensive experimental and theoretical efforts have been made to study nuclei in the proximity of Z = 40 (or 38) shell gap. Such studies have been instrumental in exploring single-particle excitation across Z = 40 and N = 50 shell closure at low spin and the emergence of collectivity due to intruding high-j orbitals at comparatively higher angular momentum [6, 7, 9, 10, 132, 145–149]. The low-lying states have been frequently described within the framework of the shell model using a ^{78}Ni core and the valence nucleons. The vital role is especially played by the protons which are hosted in $p_{3/2}, p_{1/2}, f_{5/2}, g_{9/2}$ orbits. For the states at high and medium spins and higher excitation energies, the core breaking of either Z = 40 or N = 50 shell closure is essential in generating angular momentum [149, 150]. Another indicator of such excitation is the sudden occurrence of parity changing multipole transitions. Such an enhanced $E1$ is observed in ^{94}Ru [151] and comparatively strong $M2$ transition reported in ^{93}Nb, however without much insight [132, 152]. At high-spin states, the contribution of the $g_{9/2}$ proton orbitals becomes quite essential, since the proton Fermi surface is surrounded by high-j $g_{9/2}$ intruder orbital in conjunction with low-j fp orbitals that naturally leads to structural hindrances. This should lead to the observation of isomeric states which may offer further critical insights into the structure of these excited states at low spin [81, 135, 153]. Such isomers have been extensively studied in this mass region which revealed various structural aspects such as coupling of single particle with the core, estimation of single-particle energies, contribution of nucleons through g factor measurements and so on. However, the information on the high-spin isomers is very scarce. This is in contrast to the observation of the shape isomers reported at high-spin states in $N = 83$ isotones for $A = 150$ region [154–157]. Even though, a few instances of the evolution of long-lived ($\sim$ μs order lifetime) isomers are reported at relatively non-yrast high-spin states in ^{93}Mo [11], ^{93}Nb [152], ^{87}Y and ^{89}Nb[158], it is evident from the previous literature that a comprehensive understanding of such states is yet to be formulated. The observed smooth variation of deformation parameters across the isomeric spin range in $A = 90$ led to the conclusion that the origin of such isomers should be different from those of the $A = 150$ region.

Apart from the evolution of non-yrast isomeric states at high spin, yrast bands provide rich information on nuclear shapes. Collective rotational structures emerging mostly in the form of regular dipole bands with enhanced $M1$ have been reported in many nuclei in this mass region [10, 131, 132, 159]. Interestingly, $M1$ dipole bands in ^{89}Zr represent the classically forbidden rotation of the nucleus about the long axis [131]. In fact, cranked Nilsson Strutisky calculation results for shape transition as a function of angular momentum in the favored configuration highlight evolution of various shapes throughout the spin range of the entire band. Finally, the band was found to be stabilized by the shape generated through rotation of the nucleus about the longest principal axis.

Later, an oblate collective rotational dipole band was proposed in ^{93}Nb [132] along with the prediction of an isomeric decay lifetime of 1.5(5) μs using the Doppler shift method. However, only a speculation could be made that the isomer should exist above the $37/2^{(-)}$ level. It is to be mentioned that the deformed independent particle model (DIPM) was used to determine the negative value of the axial deformation parameter for the band head level. To further justify the oblate band in ^{93}Nb similarity of$\hbar^2/2\mathscr{J}$ $\sim$ 10 keV in ^{93}Nb with that of$\hbar^2/2\mathscr{J}$ $\sim$ 15 keV measured for the negative-parity dipole band in ^{131}La, was taken to be the benchmark to claim similarity in the moment of inertia of the two nuclei. It is to be highlighted that the corresponding band in ^{131}La was already reported to be an oblate collective band [160]. It is to be iterated that the observed results in ^{131}La were discussed in the light of various observables that justify the collective oblate shape for the desired band. Further, the observation was supported by detailed cranked shell model calculations in ^{131}La. Owing to the lack of such treatments in ^{93}Nb, it is important to scan the entire band before we conclude the shapes.

In addition, doppler shift analysis was applied to conclude that all the transitions across the dipole band in ^{93}Nb were emitted within a time interval of 1.3 ps after the production of the states. This estimate on the lifetime sets a lower bound of 0.5 W.u. (= 1.7905 × 0.5 $\mu_N{}^2$ or 0.8952 $\mu_N{}^2$) on the transitional probability $B(M1)$. On the basis of $B(M1)$ value, it is claimed that the referred band is based on enhanced $M1$ transitions. The reported transition probability in ^{93}Nb is comparatively smaller than that reported for each state in the dipole band of ^{89}Zr using the DSAM method. Similarly, DSAM was applied on ^{90}Y to determine the mean lifetime of the levels in the dipole band. The order of the lifetime is comparable to ^{93}Nb and drops slightly at higher spin state [6].

To investigate the evolution of nuclear deformation within the A $\sim$ 90 regions, we measure the lifetimes of excited states in the ^{93}Nb nuclei through the Doppler Shift Attenuation Method (DSAM). The results were subsequently compared with the cranked Nilsson-Strutinsky calculations, utilizing the Potential Energy Surface (PES) method, to interpret the measured lifetimes and draw conclusions about the underlying nuclear shapes. The detailed analysis of the core excited states involving both the isospin counterparts as well as the existence of enhanced parity changing multipoles should provide testing grounds for the theoretical groups to delve into the tensorial component of nucleon-nucleon interaction.

5.2 Experimental details and analysis

High-spin states in the ^{93}Nb have been populated using the reaction ^{80}Se(^{18}O, p4n)^{93}Nb at a beam energy of 99 MeV. The ^{18}O beam from 14UD pelletron-linac accelerator was bombarded on 1.4 mg/cm^2 ^{80}Se with a backing of 1.5 mg/cm^2 ^{27}Al. The γ-rays were detected with the Indian National Gamma Array (INGA) at TIFR [61]. In the present work, three clover detectors were kept each at 157° and 140°, whereas two and four detectors were placed at 115° and 90°, respectively. Only one detector was positioned at 65°. All the angles were measured with respect to the beam direction.

The time-stamped data were collected with two- and higher-fold coincidence conditions using an XIA-based digital data-acquisition system [138].

Conventionally, the DSAM is implemented for a thin target (here ^{80}Se) deposited on a high-Z elemental backing material (here aluminium was used to have better staggering). The energy loss of the recoiling nuclei should predominantly occur in a single medium. This is ensured by the application of a thin target. Further, the use of an elemental backing medium reduces the uncertainties on the stopping simulations. The Doppler broadened γ-ray lineshapes are analyzed using the program LINESHAPE developed by Wells and Johnson [80]. The first step of the calculation consists of a Monte Carlo simulation. The simulation consists of 5000 histories of nuclei recoiling through the target and backing materials. The simulation is performed with a time step of 0.005 ps. The electronic stopping powers were calculated using the tables of Northcliffe and Schilling [78]. In the second step, the time-dependent velocity profile as observed by the detector is calculated. The calculation uses the velocity distributions obtained from the first step of the calculation and the stopping powers. The intensities of the side-feeding transitions into each level were obtained from the difference in measured intensities of the γ-ray transitions populating and depopulating the level of interest.

In the line-shape fitting procedure, the experimental lineshapes at the forward 65°, 90° and the backward 157° angles were fitted for the quadrupole band whereas fitting was dones at the backwards angle of 140° and 90° for the dipole band simultaneously with the simulated lineshapes. During the fit, in-band and side-feeding lifetimes, the background, and the contamination parameters corresponding to each transition were allowed to vary. The fittings were initiated with the top most transition of a cascade. The effective lifetime across the highest level was then fixed and in turn, used as the in-band feeding time for the next lower level. In addition, a global fit was done for all the transitions of a cascade with independent in-band and side-feeding lifetimes. At last, the lifetimes were measured by fitting the calculated line shape with the experimental spectra that correspond to the minimum χ^2 value. The uncertainties quoted for the lifetimes are obtained from the MINOS subroutine of the LINESHAPE program and do not include systematic errors from the uncertainty in the stopping power, which may vary up to 15%. The reduced transition probabilities, $B(E2)$, and $B(M1)$, were calculated from the measured level lifetime τ , using the standard relations [47].

5.3 Results and Level Scheme

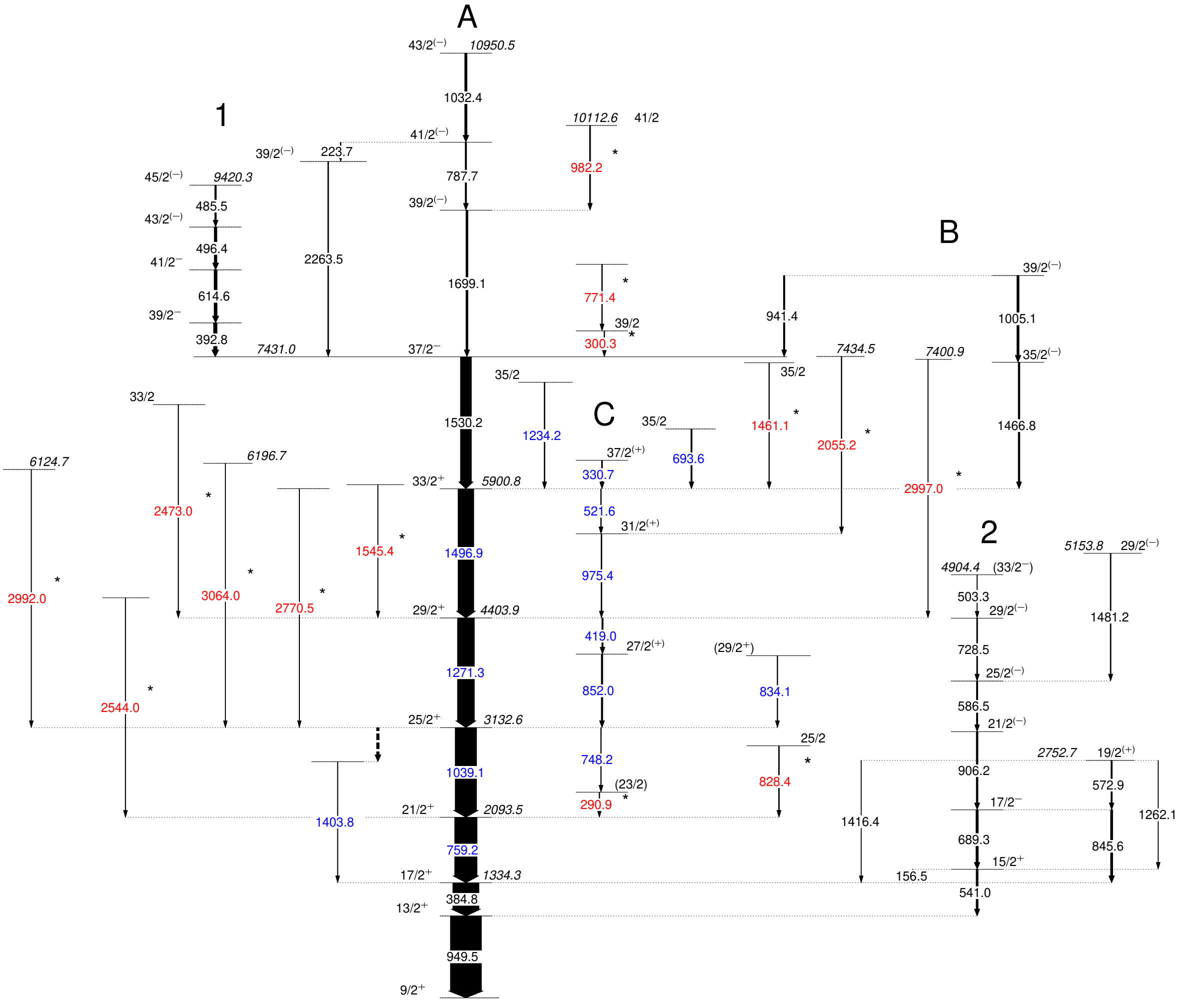

Figure 5.1 The partial level scheme of ^{93}Nb. Newly observed gamma transitions are marked by an asterisk and labelled in red color while rearranged transitions are indicated in blue. The thickness of the arrow represents the relative intensity of the gamma rays as mentioned in Table A.4.

The partial level scheme of ^{93}Nb is shown in Fig. 5.1. The entire level scheme is established on the basis of information of γ-γ coincidence and intensities of the respective γ transitions. The width of the arrows across each transition is a measure of its relative intensity with respect to 384.8-keV γ ray, whose intensity has been normalized to 100. Spin assignments have been done on the basis of multipolarity measurements which are obtained through angular distribution ratios. In some cases,

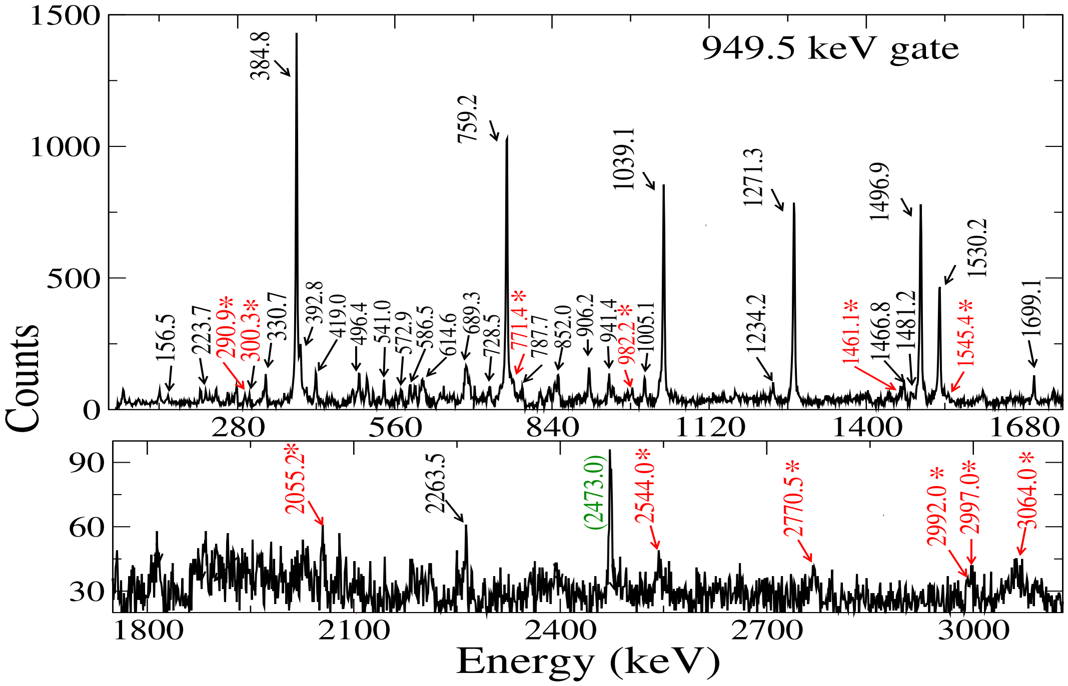

Figure 5.2 γ-γ coincidence spectrum gated on 949.5-keV transition. Transitions (in red color) marked with * are newly observed ones. The peak with parentheses in green color is contamination.

the presence of interconnecting transitions or parallel feeding patterns to other levels becomes instrumental in confirming the spin or parity of the state. Parity assignment is done by determining the polarization asymmetry parameter (see below). The details of the γ-ray energies, intensities along with angular distribution ratio, multipolarities and spin assignments are provided in Table A.4.

An overall agreement is seen between our findings related to the level structure of ^{93}Nb with the previous reports [132, 152], however, with some rearrangements in the placement of γ transitions, observation of a few new transitions, determination of spin and parities of levels where tentative assignments were done earlier. The level scheme was extended by the placement of around nine high-energy and low-intensity transitions at low- and medium-spin regimes. The newly placed transitions are shown in the spectrum (see Fig. 5.2) obtained by gating 949.5-keV ground state transition. Further, the placement of the newly observed transitions and intensity balance across the entire level scheme led to the rearrangement in the placement of already known gamma transitions. The desired ones are highlighted in blue color in the Fig. 5.1. The spin-parity assignments for the yrast branch A were found in agreement with the previous assignments.

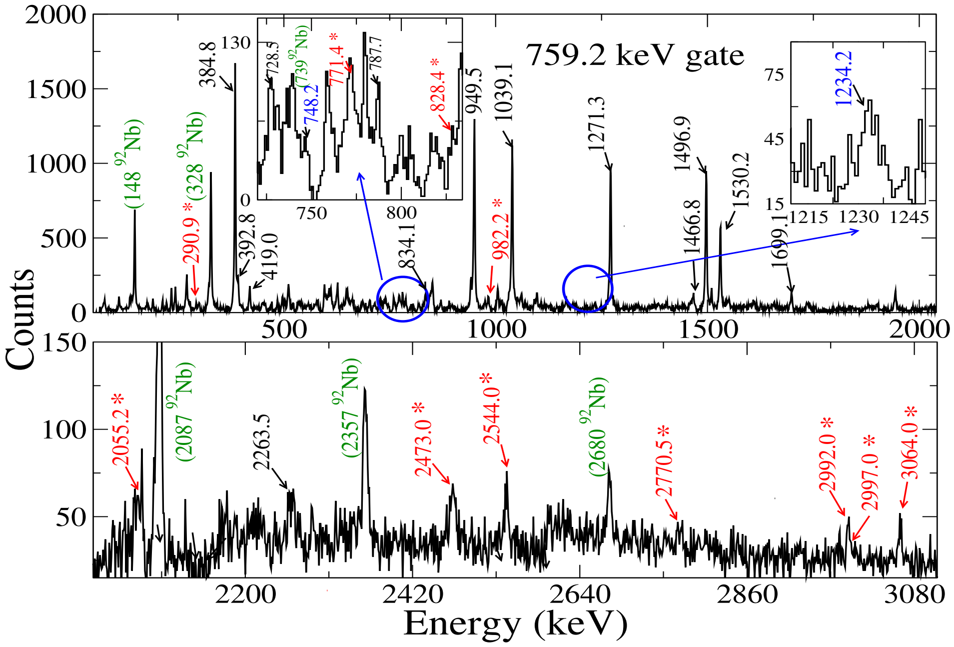

Figure 5.3 The γ-γ coincidence spectrum gated on 759.2-keV transition. Transitions in red color marked with * are newly observed ones. Peaks with parentheses in green color are contaminated peaks from nuclei ^{92}Nb.

The transition with energy 2544.0 keV is placed on top of the 21/2$^+$ state. The transition is clearly visible in the gated spectrum of 759.2 keV shown in Fig. 5.3. On the contrary, the 2544.0-keV γ ray is not observed in the spectrum generated by gating on the 1039.1-keV transition that decays from 25/2$^+$ (Fig.5.4). These arguments justify the placement of 2544.0-keV. Owing to the low intensity of the transition, spin and parity assignment could not be done for the depopulating level. A new transition with energy 828.4 keV is placed as a side feeding transition to 21/2$^+$. Multipolarity could not be measured across the γ ray. The sequence containing 748.2- and 290.9-keV transitions are placed as a parallel cascade to 1039.1-keV γ-ray. These two transitions are highlighted in the topmost panel of Fig. 5.3. When checked in the gated spectrum of 1039.1 keV, these transitions were not observed. This justifies the placement of the sequence parallel to 1039.1-keV γ ray (Fig. 5.4).

The state 25/2$^+$ is populated by 2992.0-, 3064.0- and 2770.5-keV transitions which are among the newly observed ones. The spectrum Fig. 5.5 (a) clearly shows the presence of the above-mentioned transitions in the gated spectrum of 1039.1-keV transition. All these three transitions are sufficiently weak for the determination of the multipolarity. However, these transitions were not

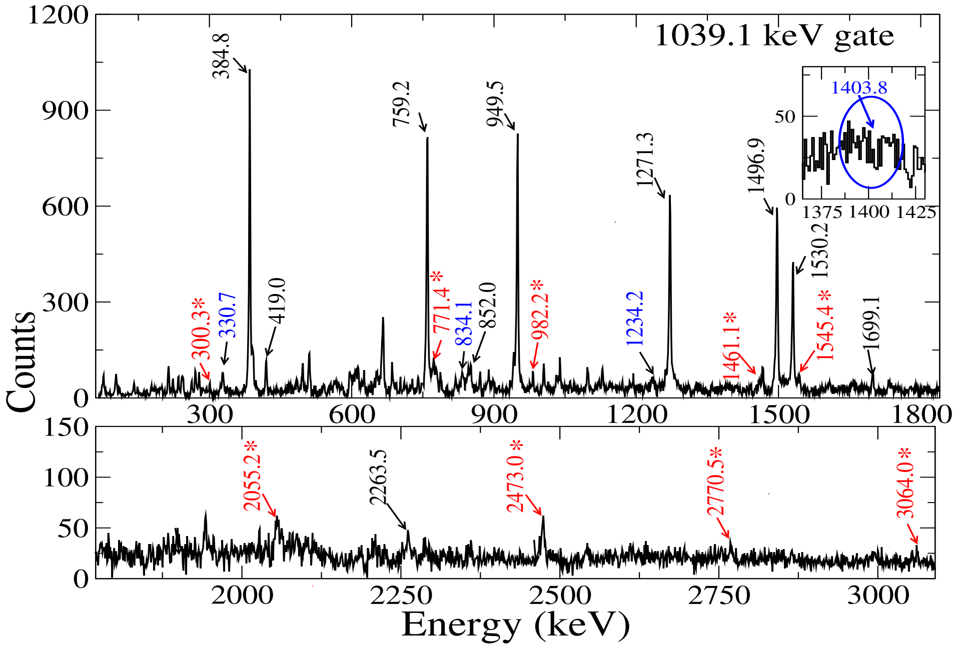

Figure 5.4 The γ-γ coincidence spectrum gated on 1039.1-keV transition. Transitions in red color marked with * are newly observed, and those in blue are shuffled to the new positions.

visible in the gated spectrum of 1271.3 keV (shown in Fig. 5.5 (b)). In addition, 1271.3-, 852.0- and 834.1-keV γ rays also feed the 25/2$^+$ level. These transitions were already reported, but the placement of all three transitions has been revised in the present work. Justification can be drawn from the presence of these transitions in the 1039.1-keV gate shown in Fig. 5.4. The transition 419.0 keV feeds on top of the 852.0-keV transition while forming an alternative cascade between 29/2$^+$ and 25/2$^+$ than the yrast 1271.3-keV decay. The multipolarity measurement tentatively suggests $M1$ character of 852.0- and 419.0-keV transitions.

Similarly, the state 29/2$^+$ is fed by newly observed 2473.0-, 1545.4- and 2997.0-keV transitions. The placement is evident from Fig. 5.5(b) where the gated spectrum of the 1271.3-keV transition endorses the presence of the above-mentioned transitions. The ADO measurements justify the dipole nature of the 2473.0-keV transition. However, owing to weak intensity, polarization asymmetry could not be measured for these transitions. In addition, 1496.9- and 975.4-keV transitions are found to feed the 29/2$^+$ level after the rearrangement in the placement. The sequence consisting of 521.6- and 975.4-keV transitions is placed as an alternative decay path to the 1496.9-keV γ ray depopulating 5900.8-keV state. The gated spectrum of 1496.9-keV transition justifies the

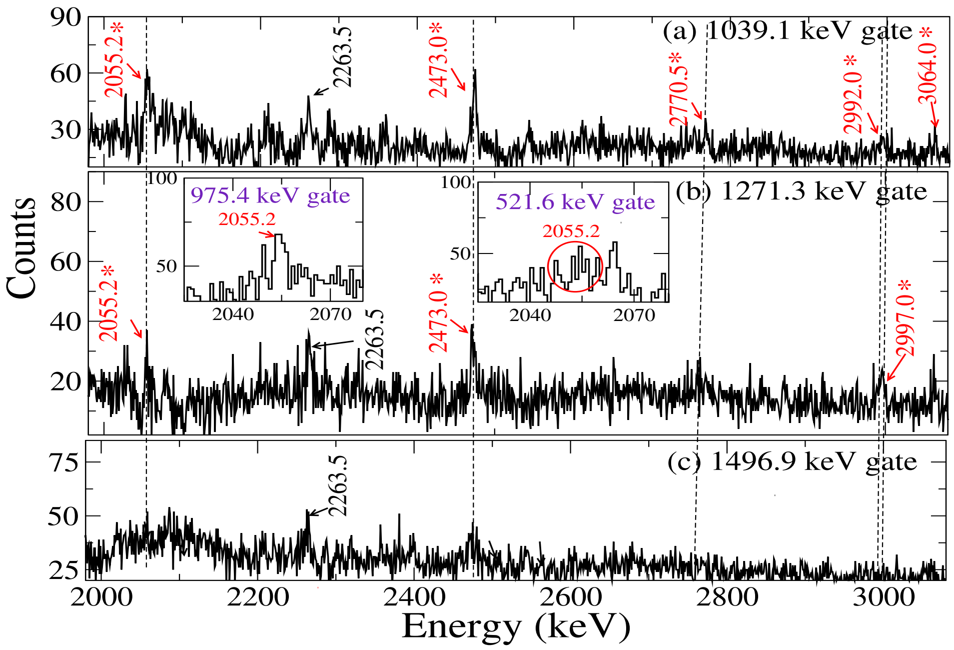

Figure 5.5 The γ-γ coincidence spectrum gated on (a) 1039.1- ,(b) 1271.3- ,and (c) 1496.9-keV transitions. Transitions in red color marked with * are newly observed ones.

placement (Fig. 5.6). Two new transitions with the high energy of 1461.1 and 2055.2 keV were found in coincidence with 521.6/1496.9- and 975.4-keV transitions respectively and hence placed accordingly (see Fig. 5.5(b)).

The transition 1530.2 keV depopulates $37/2^{-}$ state and decays at 5900.8-keV level. The transition turns out to be a quadrupole along with a parity-changing transition as per the polarization asymmetry measurements. This is in agreement with the previous assignments reported for 1530.2-keV γ ray.

Above the $37/2^{-}$, the yrast band is extended by the placement of three transitions with energy 1699.1, 787.7, and 1032.4 keV. The R_{θ} values for 787.7-, and 1032.4-keV decays agree with the previously suggested dipole nature of the transitions. However, 1699.1 keV is assigned dipole character contrary to the previously proposed quadrupole nature. A new level was observed at 10112.6 keV that decays on top of 1699.1-keV γ ray through the emission of 982.2 keV. A cascade containing 2263.5- and 223.7-keV transitions was observed to depopulate $41/2^{(-)}$ state to $37/2^{-}$ where R_{θ} value for 223.7 and 2263.5 keV confirms the dipole nature of both the transitions. The multipolarities were not reported in earlier literature.

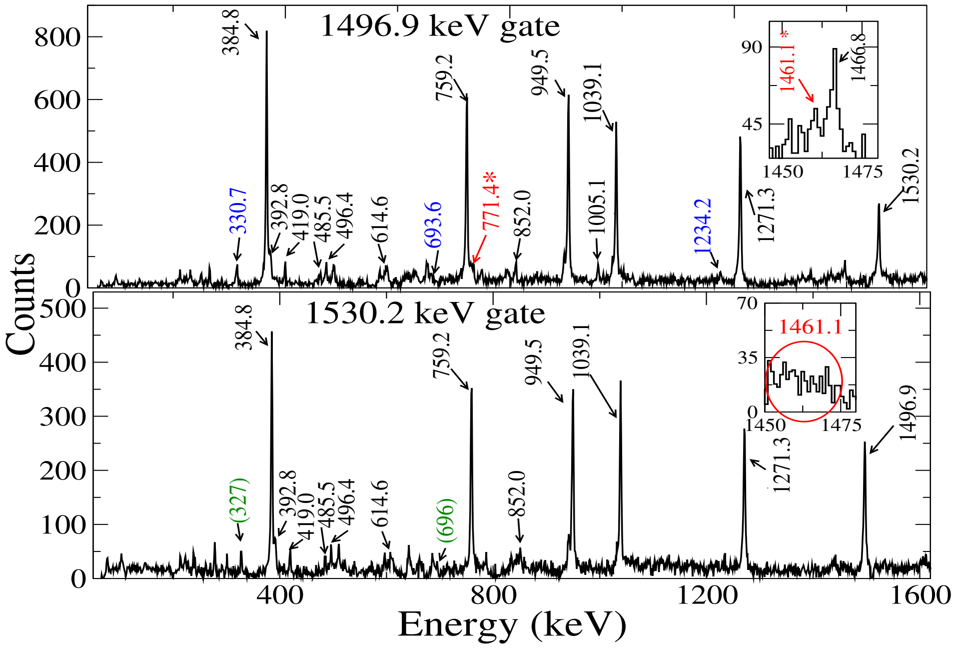

Figure 5.6 γ-γ coincidence spectrum gated on 1496.9- and 1530.2-keV transition. Transitions in red color marked with * are newly observed, and those in blue are displaced. Peaks with parentheses in green color are contamination.

As reported in the previous literature [132], a sequence (in the present work shown as band 1) consisting of four transitions 392.8-, 614.6-, 496.4- and 485.5-keV was confirmed to be in coincidence with all the transitions below the $37/2^-$ state in the yrast band. Since previously it was predicted that there exists a mirco-second isomer above $37/2^-$ level, it was necessary to ensure that the isomeric state does not intervene in the measurements related to the dipole band 1. First of all, time gates were verified with “start” at one of the transitions just above the 1530.2-keV, viz. 392.8 keV from band 1, 1699.1 keV from sequence A and 941.4 keV from sequence B and “stop” gate at 1530.2-keV transition. The time spectrum can be seen in Fig. 5.7 (a), (c), and (d) which clearly indicates a prompt spectrum centred at 2000 units of the time axis. As a measure of further verification, a time spectrum with a “start” gate at 496.4-keV γ ray from band 1 and a “stop” at 1530.2 keV was made which also produced a prompt spectrum as shown in Fig. 5.7 (b). Therefore, the predicted isomer is not present either at $37/2^-$ or band 1. Hence, ADO measurements could be applied to the transitions of the sequence. The measured ADO values confirm the dipole character of the transitions, and the results agree well with the previous reports. However, the placement of 614.6- and 496.4-keV transitions was shuffled based on the intensity of the transitions. Further,

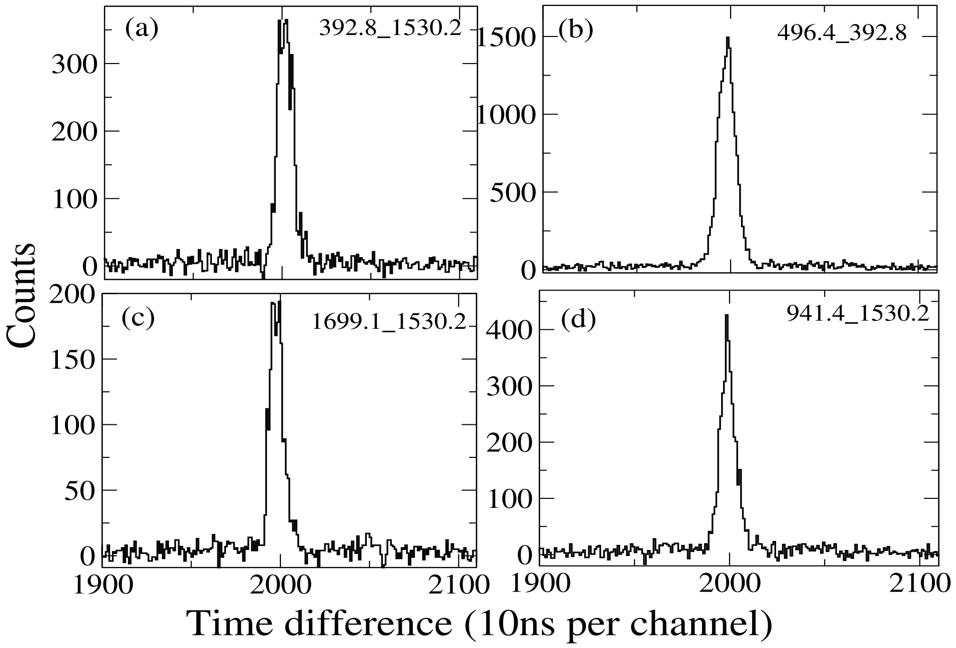

Figure 5.7 The time-difference spectra were constructed using the 392.8-, 496.4-,1699.1- and 941.4-keV transitions as a "start" and the 1530.2-, 392.8-, 1530.2-, and 1530.2-keV transitions as "stop" shown in panels a, b, c, and d respectively.

the spin and parity of the initial two levels of the sequence could be confirmed in the present work. On the other hand, only the spin could be confirmed for the top two levels of the cascade through multipolarity measurement. Therefore, the band is confirmed to be based on magnetic dipole transitions.

The sequence E (band 2 in the present work) reported by YI-Heng *et al.* [132] was reproduced in the present work. The multipolarity assignments are in compliance with the previous literature. However, as the polarization measurement could not be performed for these transitions, we adopted the parity assignments as was done by Wakabayashi *et al.* [152].

On the other hand, the transitions 476.2 and 1049.5 keV in sequence D of YI-Heng's work and the transitions 234.0, 1238.4, 1434.7, 302.2, 902.2, 1734.5 keV reported by YI-Heng *et al.* [132] are not observed in the present data. Transitions 330.7, 693.6, 748.2, 1234.8 and 1403.8 keV have been displaced according to γ - γ coincidence. The 330.7-keV transition is observed in the gated spectrum of the 1039.1-keV shown in Fig. 5.4. Additionally, the 748.2-keV transition is visible in the gated spectrum of the 759.2-keV shown in Fig. 5.3. Lastly, the 1234.8-keV transition can be observed in the gated spectra of 759.2-keV and 1039.1-keV, as depicted in Fig. 5.3 and 5.4. These spectra were used to determine the locations of the transitions. In contrast, transition 693.6 keV was not observed in the gated spectrum of 1530.2 keV (see Fig. 5.6). It has been placed parallel to the 1530.2 keV transition in the present work. Additionally, the 1403.8 keV transition was not observed in the gated spectrum of 1039.1 keV as shown in the inset of Fig. 5.4, and has been placed parallel to the 1039.1 keV transition in the present work.

5.3.1 Lifetime measurements through DSAM

The measurement of level lifetimes has been separately categorized for the positive-parity yrast quadrupole band and the negative-parity dipole band feeding on top of the $37/2^-$ state.

The Doppler-shifted spectra were generated from the asymmetric matrices with a gate on 759.2-keV γ ray. Representative lineshape spectra of 1039.1-, 1271.3-, 1496.9- and 1530.2-keV transitions observed at 157°, 90°, and 65° angles are displayed in Fig. 5.8. The top transition, i.e., 1530.2 keV, was fitted assuming 100% side feeding. In the fitting process, the lineshapes of all four transitions were fitted separately in different windows. In this analysis, we assumed the independent side feeding model for side feeding. The level lifetimes and the corresponding errors reported in Table 5.1 were obtained from the lineshape fitting of the angle-dependent Doppler-shifted spectra at the mentioned angles.

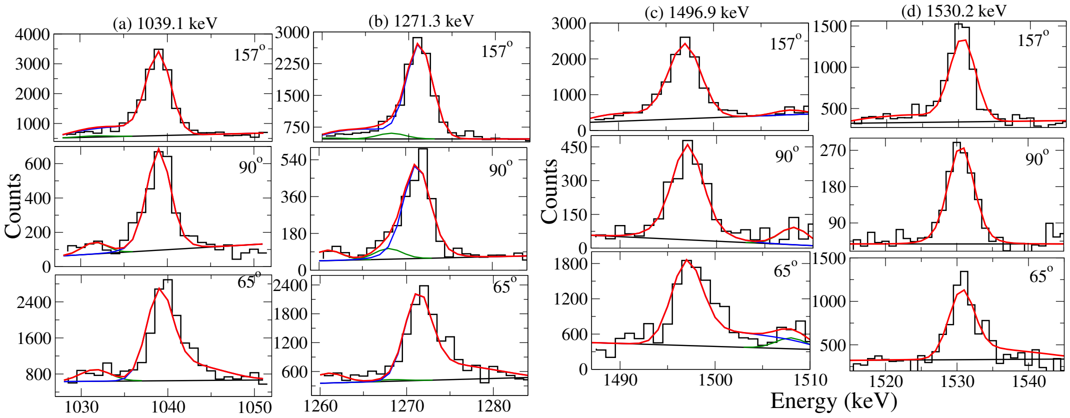

Figure 5.8 Representative spectra along with theoretically fitted lineshapes for (a) 1039.1.7 keV, (b) 1271.3 keV, (c) 1496.9 keV and (d) 1530.2 keV quadrupole transitions in quadrupole ground state band of ^{93}Nb. The top, middle, and bottom rows correspond to the shapes in the 157°, 90°, and 65° detectors, respectively. The desired lineshapes of gamma transitions, contaminant peaks, and total lineshapes are represented by the blue, green, and red curves, respectively.

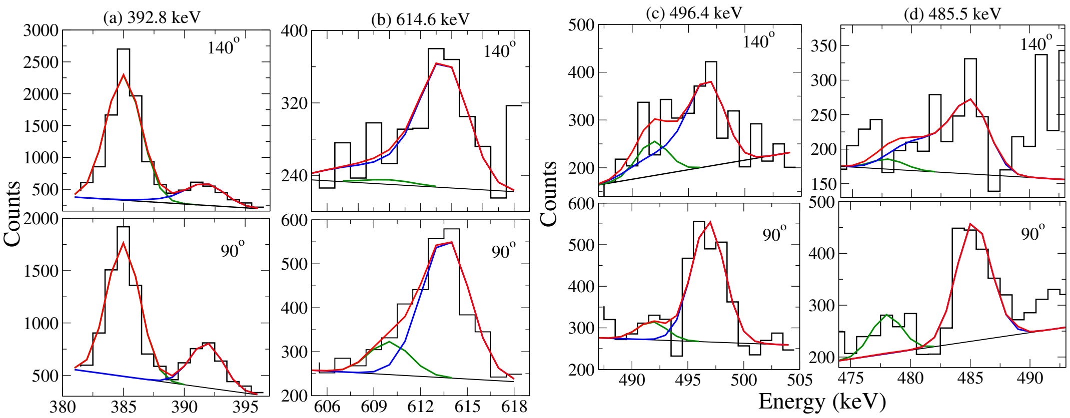

Figure 5.9 Representative spectra along with theoretically fitted lineshapes for (a) 392.8 keV, (b) 614.6 keV, (c) 496.4 and (d) 485.5 keV dipole transitions in the dipole band of ^{93}Nb. The upper and lower rows correspond to the shapes in the 140° and 90° detectors, respectively. The blue, green, and red curves represent the desired lineshapes of gamma transitions, contaminant peaks, and total lineshapes.

Table 5.1 Measured lifetimes of states in the band A consisting of quadrupole transitions, τ (ps), and corresponding reduced transition strengths. Systematic errors due to uncertainties in the stopping powers used are not included.

E_γ (keV)	$J_i^\pi \rightarrow J_f^\pi$	B.R. (%)	τ (ps)	$B(E2)^b$ $(eb)^2$
1039.1[a]	$25/2^+ \rightarrow 21/2^+$	94	$0.73^{+0.10}_{-0.11}$	$0.08^{+0.01}_{-0.02}$
1271.3	$29/2^+ \rightarrow 25/2^+$	93	$0.73^{+0.13}_{-0.07}$	$0.03^{+0.01}_{-0.01}$
1496.9	$33/2^+ \rightarrow 29/2^+$	96	$0.91^{+0.19}_{-0.12}$	$0.01^{+0.002}_{-0.002}$
1530.2	$37/2^- \rightarrow 33/2^+$	100	0.35(.03)[c]	-

[a] Branching through feeding on top of 1403.8-keV has been considered.

[b] $B(E2)expt.$=0.816(B.R/100)/(E_γ^5)τ(1+α)

where E_γ is the experimentally measured transitional energy in units of MeV, τ is the mean lifetime of the decaying level in ps, branching ratio and α taken from Table A.4.

[c] Effective lifetime is obtain assuming 100% side-feeding intensity. Hence, it is the upper limit of level lifetime (τ).

Table 5.2 Measured lifetimes of states in the $M1$ band, τ (ps), and corresponding $B(M1)$ μ_N^2 reduced transition strengths. Systematic errors due to uncertainties in the stopping powers used are not included.

E_γ	$J_i^\pi \rightarrow J_f^\pi$	Internal conversion	τ	$B(M1)^a$
(keV)		coefficient (ICC)	ps	μ_N^2
392.8	$39/2^- \rightarrow 37/2^-$	.006	$0.13^{+0.15}_{-0.07}$	$7.18^{+3.85}_{-8.38}$
614.6	$41/2^- \rightarrow 39/2^-$	.002	$0.12^{+0.14}_{-0.09}$	$2.04\ ^{+1.23}_{-2.85}$
496.4	$43/2^- \rightarrow 41/2^-$	.003	$0.17^{+0.15}_{-0.07}$	$2.72^{+1.27}_{-1.91}$
485.5	$45/2^- \rightarrow 43/2^-$	.003	0.19^b	2.61^c

$^aB(M1)(expt.)$=0.05697(B.R/100)/$(E\gamma)^3\tau(1+\alpha)$

where E_γ is the experimentally measured transitional energy in units of MeV, τ is the mean lifetime of the decaying level in ps.

^{b} Effective lifetime is obtain assuming 100% side-feeding intensity. Hence, it is the upper limit of level lifetime (τ).

^{c} Lower limit of the $B(M1)$ value.

Similarly, the Doppler-shifted spectra were generated from the asymmetric matrices with a gate on 1530.2-keV γ ray. Representative lineshape spectra of the 392.8-, 614.6-, 496.4- and 485.5-keV transitions observed at 140° and 90° angles are displayed in Fig. 5.9. We are unable to fit the shape due to insufficient data at the forward angle. The level lifetimes along with their uncertainties reported in Table 5.2 were obtained from the lineshape fitting of the angle-dependent Doppler-shifted spectra at these angles. The transition at 485.5 keV was fitted with 100% side feeding.

5.4 Discussions

The microscopic structure of nuclei in the $Z \approx 40$, $N \approx 50$ region is dominated by the $1g_{9/2}$, $2p_{1/2}$, $2p_{3/2}$, $1f_{5/2}$, $2d_{5/2}$, $1g_{7/2}$ and $1h_{11/2}$ orbitals. The high-spin states will be formed through the contribution from the $d_{5/2}$, $g_{7/2}$ and $h_{11/2}$ neutron single-particle orbitals. Large-scale shell model calculations have been extensively used to describe spin states up to high spin in this mass region [9, 10, 132, 145, 148, 149, 159]. We have witnessed striking similarity in the results obtained using single-particle as well as collective models in ^{89}Zr [131, 145]. It will be interesting to see whether such agreements are observed in ^{93}Nb. The nucleus lies slightly away from the mid-shell core and hence is likely to be dictated by strong competition between single-particle and collective phenomena.

The states in ^{93}Nb have been probed within the framework of the pairing independent cranked Nilsson-Strutinsky (CNS) model [117, 161, 162]. In this model, configurations are designated by the number of particles or holes in orbitals labelled by the N oscillator shell. Each oscillator shell is further grouped into high- and low- j shells. A further categorization is made based on the signature α = 1/2 and α = -1/2. The configurations are then labelled by the number of particles or holes in each group.

The calculations are performed with κ and μ parameters (coefficients of the $\mathbf{l} \cdot \mathbf{s}$ and $\mathbf{l}^2$ terms in the modified oscillator potential [94]) fitted for the A = 80 regions [163]. The total energy is calculated as a sum of the rotating liquid drop energy and the shell energy, while implementing the Strutinsky shell correction formalism [97, 127]. The static liquid drop reference used corresponds to the Lublin-Strasbourg drop (LSD) [164]. The rigid body moment of inertia is calculated with a radius parameter of r_0 = 1.16 fm and diffuseness of a = 0.6 fm [117]. Ultimately, the energy is minimized with respect to the axial and triaxial deformation parameters for different configurations, ε_2, ε_4, and γ respectively. The minimization is executed at different angular momenta.

The labelling of the configuration follows the nomenclature: $[p_1p_2,n_1n_2n_3]$, where p_1 is the number of proton holes in the *fp* shell and p_2 represents the number of protons in the $g_{9/2}$ shell. As well, n_1 is the number of neutron holes in the $g_{9/2}$ shell, n_2 shows the number of neutrons in *gds* orbitals, and n_3 is the number of $h_{11/2}$ neutrons. Whenever there is an odd number of particles in a group, the signature is highlighted by a subscript, "+" for α = 1/2 and "-" for α = -1/2 that provides a complete description of the configuration.

In the following, we will discuss the results of the model calculation. Calculations were performed to extract energetically favored configurations that should be ideally suited to describe the observed bands in ^{93}Nb. The calculated the lowest energy configurations are shown in Fig. 5.10, where the excitation energy over and above the energy of a rotating liquid drop across each configuration was followed as a function of spin. The results are then separately compared with different configurations for the experimental observations respectively.

The ground state positive-parity band A was found to agree well with the configuration $\pi((fp)^{-2}g^3_{9/2}) \otimes \nu(g^0_{9/2}(gds)^2)$ [23_+;02] as the difference in excitation energy relative to rotating liquid drop mostly stays around zero value over the required spin range till 33/2 $\hbar$. Earlier literature also suggested similar configurations with $\pi((fp)^{-2}g^3_{9/2}) \otimes \nu(d_{5/2})^2)$ based on the shell model calculations. This is encouraging to witness the agreement between the single-particle model and the collective model. In order to build an understanding of the nuclear shapes, stable minima in potential energy contours for the given configuration were followed in the spin range (6.5$\hbar$ to 16.5$\hbar$) (see Fig. 5.11). Initially, the nucleus attains a triaxial shape with $\varepsilon_2 \approx$ 0.12 and $\gamma \approx$ -30°. At the spin 10.5 $\hbar$ (i.e. 21/2$^+$, the coexistence of two shapes is observed with one favored non-collective oblate and another prolate deformed shape at $\varepsilon_2 \approx$ 0.1. Beyond this state, the prolate becomes favored before the configuration terminates at 14.5$\hbar$ and 16.5$\hbar$. We see that favored terminating states at 10.5$\hbar$ and 14.5$\hbar$ can also be concluded from the downsloping

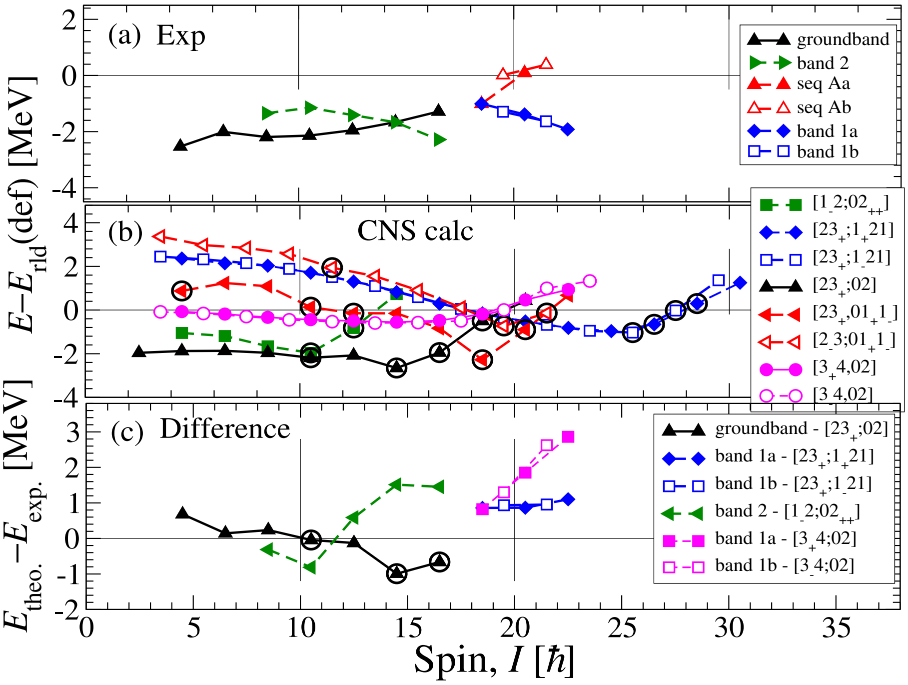

Figure 5.10 Excitation energies relative to rotating-liquid drop energy as a function of angular momentum, for observed (panel a) and calculated (panel b) valence-space states for ^{93}Nb. The difference between the observed and calculated results has been shown in panel c. The closed and the open circles represent the (α = +1/2) and the (α= -1/2) states respectively. The positive parity configuration is shown by solid lines whereas the configurations with negative parity are drawn with broken lines. Aligned states are encircled.

curve in panel (b) of Fig. 5.10. This should be the underlying reason that a few high-energy γ rays are observed to decay at $10.5\hbar$ and $14.5\hbar$ levels, respectively. However, $16.5\hbar$ (or $33/2^+$) should be an unfavored terminating state.

Let us understand the generation of these terminating states with the help of sloping Fermi Surface diagrams shown in Fig. 5.12. The highest-spin states in valence configurations with neutrons in *gd* orbital are formed from the valence particles as

$\nu(d_{5/2}^2)$, $I = 0\hbar$ for a couple of anti-aligned neutrons in $d_{5/2}$,

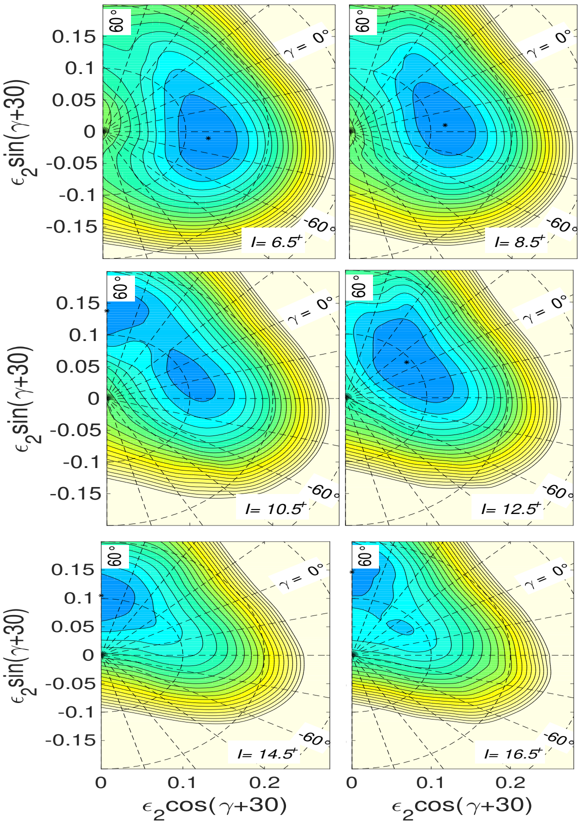

Figure 5.11 Calculated total energy surfaces for spin 6.5$\hbar$ to 16.5$\hbar$ [23;02] ground band configuration for band A in ^{93}Nb. The contour line separation is 0.25 MeV.

$\nu(d^2_{5/2})$, $I = 4^+$ with the pairing broken,

$\nu(g_{7/2}d_{5/2})$, $I = 6^+$ with each neutron occupying $g_{7/2}$ and $d_{5/2}$ respectively.

When combined with the favored aligned proton structure

$\pi((fp)^0 g^3_{9/2})$, $I = 21/2^+$,

they give rise to low-lying states with $21/2^+$, $29/2^+$ and $33/2^+$, respectively.

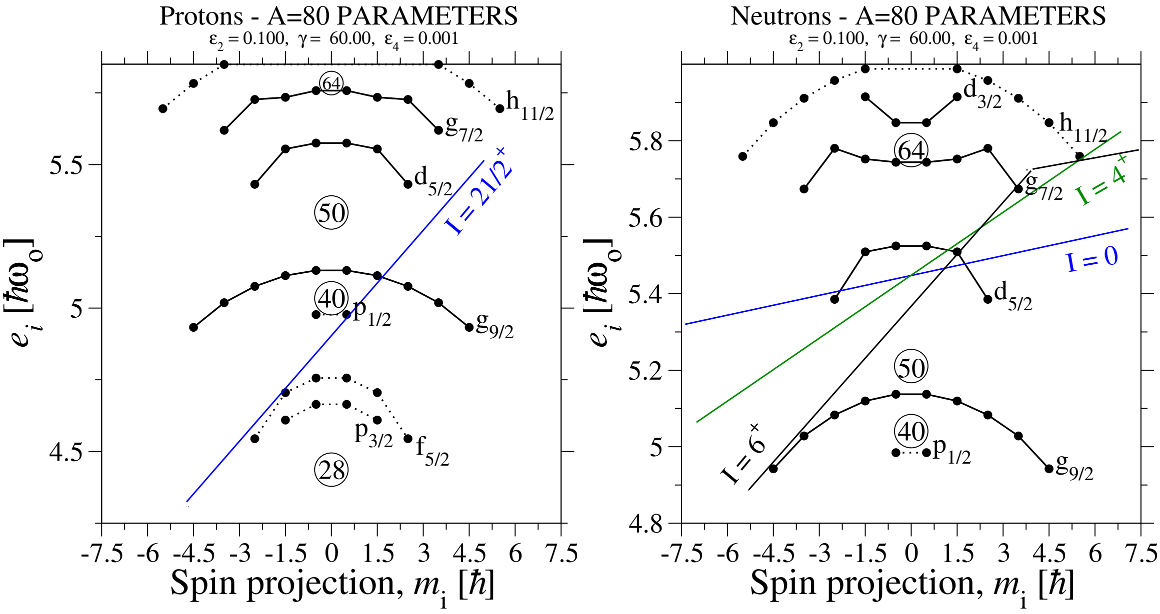

Figure 5.12 Calculated sloping Fermi-surface plots. Representing the maximum spin state in $[23_{+};02]$, configuration in ^{93}Nb.

It is interesting to notice that the $21/2^{+}$ state acts as an anti-aligned state. Similar states were reported in $A \sim 120$ [165–167]. Anti-aligned states are in general energetically favored states just like the aligned states and therefore, such levels are stabilized with non-collective oblate shapes. To generate higher angular momentum, the anti-aligned pair should be broken which should lead to a gradual build-up of angular momentum. A similar phenomenon should also take place at partially aligned states like that of $29/2^{+}$. Contrary to the formation of a smooth band, several high-energy γ transitions were observed to feed the anti-aligned state at $I = 21/2^{+}$ and partially aligned state at $I = 29/2^{+}$. The large transitional energy of the γ rays feeding the $I = 21/2^{+}$, $29/2^{+}$, lie between $\approx$ 1.5 and 3.0 MeV which indicates the possibility that these transitions de-excite the core-breaking states [167, 168]. They may involve neutron excitation across the $N = 50$ magic numbered shell gap from $(g_{9/2})$ into $(g_{7/2}, d_{3/2}, s_{1/2})$ or $h_{11/2}$ orbitals. On the other hand, transition energy close to 3.0 MeV may stem out of levels based on proton excitation across the $Z = 40$ semi-magic shell closure from $(f_{5/2}, d_{5/2})$ into $(g_{9/2})$ orbital. In fact, such states were recently observed in ^{90}Zr which happens to be the semi-magic nucleus [8]. In ^{90}Zr, a band consisting of high-energy γ rays was observed to feed the fully aligned 8^+ state. The band was described to be based on neutron core-excited states. Furthermore, similar observations were also made in $^{90-91}$Nb [149, 169]. A level with an energy of 4.3 MeV was observed at $21/2^+$ in ^{91}Nb. It is straightforward to have major contributions from the configurations $\pi[(2p_{1/2})^{-2}(1g_{9/2})^3]$ and $\pi[(1f_{5/2})^{-2}(1g_{9/2})^3]$ towards $21/2^+$ [149] with null contribution from all paired up neutrons at magic number 50. The positive parity states decaying to $21/2^+$ though, coincident high-energy transitions were described by proton excitation. Therefore, it can be concluded that this mass region is enriched by states built upon either neutron- or proton-core excitation. Thus, the anti-aligned $21/2^+$ state in ^{93}Nb with no neutron contribution turns out to be a replica of the $21/2^+$ level in ^{91}Nb. Similarly, neutron excitation beyond $N = 50$ shell gap can be coupled with the nucleonic occupancy of $29/2^+$ to describe the high-energy states de-exciting to the level via high-energy γ rays in ^{93}Nb. The possibility of coupling of neutron- and proton-core-excited configurations should not be denied too, as that may be the cause of the observation of high-energy transitions feeding to intermediate levels like $25/2^+$.

Till now, the underlying configurations of the observed ground state band were being discussed through a comparison of excitation energy and spin (eigenvalues) of the calculated configurations. However, feasible wavefunctions involved in generating the observed states can only be ascertained through a comparison of calculated $B(E2)$ values with the corresponding measured values. The transitional quadrupole moment (Q_t) can be extracted using the CNS model, which can be correlated with $B(E2)$. For $\Delta J = 2$ transitions, the reduced transition probability within a band with fully aligned spin can be written as [170–172]

$$B(E2; I, K = I \rightarrow I-2, K = I-2)$$
$$= \frac{5}{16\pi} \langle I, I; 2, -2 | I-2, I-2 \rangle^2 \, Q_t^2$$

The calculated $B(E2)$ for $25/2^+ \rightarrow 21/2^+$ comes out to be 0.08 $(eb)^2$ corresponding to $Q_t = 0.99$ *eb*. This agrees very well with the measured $B(E2)$ of $0.08^{+0.01}_{-0.02}$ $(eb)^2$. The subsequent values in Table 5.1 for $29/2^+ \rightarrow 25/2^+$ and $33/2^+ \rightarrow 29/2^+$ could not be directly compared with the results from CNS calculations because the states at $29/2^+$ and $33/2^+$ happen to be anti-aligned or aligned states. However, the observed $B(E2)$ value for $29/2^+ \rightarrow 25/2^+$ drops to $0.03^{+0.01}_{-0.01}$ $(eb)^2$ which is less than half of the value across $25/2^+ \rightarrow 21/2^+$ whereas in case of $33/2^+ \rightarrow 29/2^+$ it further drops to $0.01^{+0.002}_{-0.002}$ $(eb)^2$. This concludes that the assigned configuration $[23_+;02]$ should successfully describe the building of angular momentum across the ground state band. The next transition 1530.2 keV has a dominant $M2$ character. In general, $M2$ dominant decays are hindered. However, the measured lifetime across 1530.2 keV is 0.35 ps. Dieter Kurath and R. D. Lawson have advocated for such favored $M2$ transitions by stating that the residual nucleon-nucleon force can create an eigenfunction in the hole state where the hole state couples with both the ground state configuration of the core nucleus as well as one of the nearby excited states also, thereby compelling these components to interfere destructively in the matrix element [173].

As discussed in the experimental results, a dipole band (band 1) consisting of four transitions feeds at $37/2^-$. The measured $B(M1)$ values across each level in the band indicate enhanced $M1$ character of the corresponding depopulating transitions. It is to be noted that no regular trend was observed in the variation of $B(M1)$ across the band as a function of angular momentum. Similar near-constant values of $B(M1)$ were measured by Saha *et al.* [131] in ^{89}Zr at around similar angular momentum. In addition, Rainovski *et al.* also confirmed constant $B(M1)$ across the transitions in the observed dipole band in ^{90}Y.

Later, similar constant $B(M1)$ values were also measured for the isotopes of Mo [174]. It is interesting to realize that the above-mentioned isotopes, including ^{93}Nb lie close to the semi-magic shell closure at ^{90}Zr and may showcase favorable configurations at the ground state or excited state to conform to magnetic rotation. However, such a phenomenon has not been observed to date for any of the nuclei wherever explicit lifetime measurements were done for such bands. As mentioned for ^{89}Zr [131] and ^{141}Nd [175], it is also likely in ^{93}Nb that the rotation axis is tilted, which leads to stronger $M1$ transitions. As discussed in [175], this will only have minor perturbative effects on the energies but lead to an increased $M1$ transition strength.

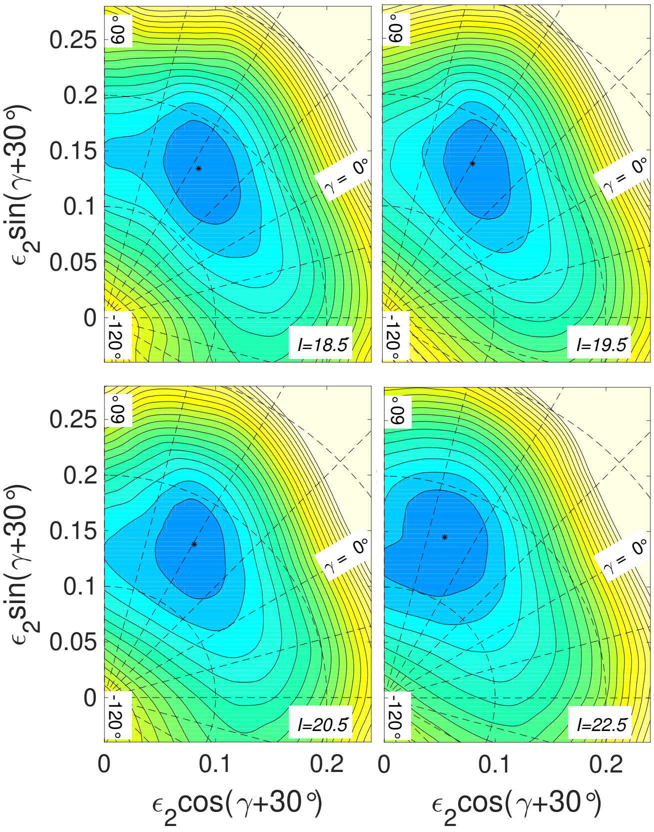

Figure 5.13 Calculated total energy surfaces for 18.5 $\hbar$, 19.5 $\hbar$, 20.5 $\hbar$ and 22.5 $\hbar$ for [23;121] band 1 in ^{93}Nb.

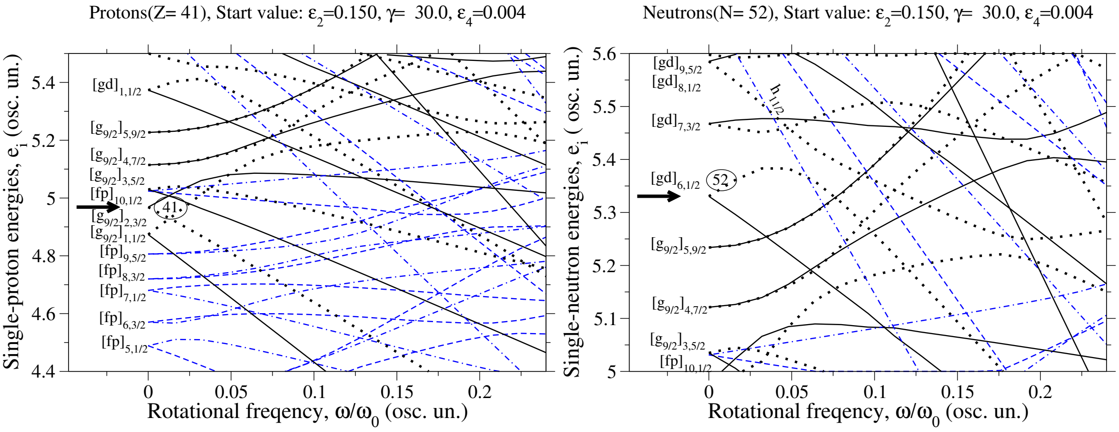

Figure 5.14 Single particle Routhians for protons (a) and neutrons (b) typical triaxial deformation parameters $\varepsilon_2 = 0.15$, $\gamma = 30^\circ$ and $\varepsilon_4 = 0.004$. Four combinations of different (π, α) are plotted with the following representation: solid lines are for (+, +1/2), dotted lines represent (+, -1/2) whereas (-, +1/2) and (-, -1/2) are shown by dashed and dashed-dotted lines respectively. The labelling of the orbitals is done for zero rotational frequency. $[fp]$ and $[gd]$ represent the orbitals with dominant amplitudes in and $(p_{1/2}, p_{3/2}, f_{5/2})$ $(g_{7/2}, d_{5/2})$ respectively with the ordering and Ω-values as subscripts. The black thick arrow signifies the position of the Fermi level. For clarity, the number of nucleons are mentioned at the zero rotational frequency.

The observed dipole band develops smoothly with spin which means that one should be able to find energetically favorable calculated configurations at spins where the band is populated. This clearly indicates that the even spin states of the observed band should be assigned to the [23_+;1_+21] configuration which behaves smoothly in an extended spin range I = 18.5-21.5$\hbar$. On the contrary, the signature α = -1/2; i.e, odd-spin sequence should subsequently be assigned the [23_+;1_-21] configuration, i.e. with a different signature for the $g_{9/2}$ neutrons. It was ensured that these two signature partners of the same calculation configuration $\pi((fp)^{-2}g^3_{9/2}) \otimes \nu(g^{-1}_{9/2}(gds)^2)h^1_{11/2}$ remains low in excitation energy at the desired spin range. The same is shown in Fig. 5.10 (b) as blue diamonds (closed and open symbols, respectively). Corresponding energy contours as a function of deformation parameters are shown in Fig. 5.13. Potential energy surfaces (PES) have been shown for four spin states at 18.5, 19.5, 20.5, and 22.5$\hbar$. The nucleus is stabilized via triaxial shape with ε_2 = 0.15 and γ = 30° across the entire dipole band. The evolution of Fermi levels at the extracted deformation within this configuration can be understood from Fig. 5.14. It observed that the configuration is dictated by the occupation of protons in low-Ω high-j $g_{9/2}$ coupled with neutrons in (gds) and low-Ω $h_{11/2}$ orbitals. This should drive the nucleus to rotate about the longest principal axis. However, the high-Ω proton and neutron holes in fp and $g_{9/2}$ respectively, present a competition by inducing rotation about the short/intermediate axis. This difference in respective orientations due to particles and holes may be a cause of large transverse $M1$ transitions as explained in [175]. Therefore, it is concluded that the dipole band with enhanced $M1$ character is an outcome of neutron core-excitation across N = 50 closure. A similar description of the negative-parity dipole bands can be found for ^{91}Nb, where, a couple of such bands were explained through neutron excitation beyond N = 50 magic core except for the highest spin states where proton excitation from fp shell to $g_{9/2}$ orbital was shown to be favored [135]. On the other hand, Yi-Heng Wu *et al.* has interpreted this dipole band involve excitation of three proton holes in fp shell along with four protons in $g_{9/2}$ that couple with neutron occupancy within N = 50 core [132]. We analyzed this configuration within the framework of CNS calculations. The excitation energy with respect to a rotating liquid drop as a function of spin was calculated and plotted for the configuration (see the pink curves in Fig. 5.10 panel (b)). As the spin increases, instead of converging to a minimum in energy, the configuration shoots upward towards unfavorable higher energy. A similar trend is displayed while comparing the experimental excitation energy with that of the calculated one (Fig. 5.10 panel (c)). Therefore, it seems justified to include the neutron excitation across N = 50 shell closure so as to have favorable excitation energy for the dipole band. It is further mentioned that the $B(E2)$ values across either of the α = +1/2 or -1/2 for $\pi((fp)^{-2}g^{3}_{9/2}) \otimes \nu(g^{-1}_{9/2}(gds)^{2})h^{1}_{11/2}$ is calculated to be excessively low than the measured $B(M1)$ values across the dipole transitions.

Band 2 is another sequence built with negative parity states. Yi-Heng Wu *et al.* has proposed $\pi(p^{-1}_{1/2}g^{2}_{9/2})\otimes\nu(d_{5/2})^{2}$ for $17/2^{-}$ and $21/2^{-}$ states. The states beyond $21/2^{-}$ were assigned $\pi((f_{5/2}p_{3/2}p_{1/2})^{-3}g^{4}_{9/2})\otimes\nu(d_{5/2}g_{7/2})$. In the present work, configuration $\pi((fp)^{-1}g^{2}_{9/2})\otimes\nu(g^{0}_{9/2}(gds)^{2})$ $[1_{-}2;02_{++}]$ is assigned to the band 2. This agrees well with the earlier assignment. Potential energy surfaces were drawn for I = 8.5, 10.5, 12.5 and 14.5$\hbar$ (see Fig. 5.15). The nuclear shape is stabilized by a near-triaxial shape with $\varepsilon_2 \approx 0.15$ at medium spin. However, low spin regions are also dominated by non-collective oblate at terminating spin values.

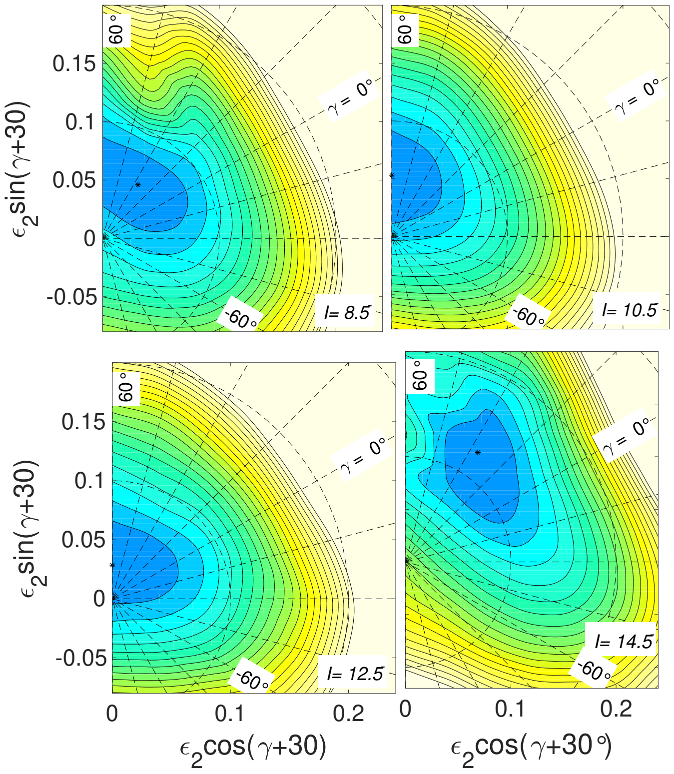

Figure 5.15 (Calculated total energy surfaces for 8.5$\hbar$, 10.5$\hbar$ 12.5$\hbar$ for [12;02] and 14.5$\hbar$ for [23;011] band 1 configuration in ^{93}Nb.

5.5 Summary

The previously known level structure in ^{93}Nb has been rearranged owing to the observation of several high-energy γ transitions decaying from single-particle excited states to the aligned or anti-aligned states in the ground state band. Such transitions have presented a unique example of neutron and proton core-excited configurations. The level scheme was further updated with the addition of a few new transitions. The dipole band based on enhanced $M1$ transitions was verified and re-investigated through the lifetime measurement of the corresponding levels using DSAM. Lifetimes were also measured for some of the $E2$ transitions in the ground state band. Extensive calculations were performed in the framework of CNS to show that the dipole band evolves with triaxial shape which is contrary to the earlier prediction of collective oblate shape.